ACS Photonics

Article

pubs.acs.org/journal/apchd5

Monolithic CIGS−Perovskite Tandem Cell for Optimal Light Harvesting without Current Matching

Paola Mantilla-Perez,*,† Thomas Feurer,‡ Juan-Pablo Correa-Baena,§ Quan Liu,† Silvia Colodrero,† Johann Toudert,† Michael Saliba,§ Stephan Buecheler,‡ Anders Hagfeldt,§ Ayodhya N. Tiwari,‡ and Jordi Martorell†,∥

†ICFO-Institut de Ciencies Fotoniques, Mediterranean Technology Park, Castelldefels 08860, Spain

‡Laboratory for Thin Films and Photovoltaics, Empa-Swiss Federal Laboratories for Materials Science and Technology, Duebendorf 8600, Switzerland

§Laboratory for Photomolecular Science, Institute of Chemical Sciences and Engineering, Ecole Polytechnique Fédérale de Lausanne, Lausanne 1015, Switzerland

∥Departament de Física, Universitat Politecnica de Catalunya, Terrassa 08222, Spain

S *Supporting Information*

ABSTRACT: We present a novel monolithic architecture for optimal light harvesting in multijunction thin film solar cells. In the configuration we consider, formed by a perovskite (PVK) cell overlying a CIGS cell, the current extracted from the two different junctions is decoupled by the insertion of a dielectric nonperiodic photonic multilayer structure. This photonic multilayer is designed by an inverse integration approach to confine the incident sunlight above the PVK band gap in the PVK absorber layer, while increasing the transparency for sunlight below the PVK band gap for an efficient coupling into the CIGS bottom cell. To match the maximum power point voltages in a parallel connection of the PVK and CIGS cells, the latter is divided into two subcells by means of a standard three-laser scribing connection. Using realistic parameters for all the layers in the multijunction architecture we predict power conversion efficiencies of 28%. This represents an improvement of 24% and 26% over the best CIGS and PVK single-junction cells, respectively, while at the same time outperforms the corresponding current-matched standard tandem configuration by more than two percentage points.

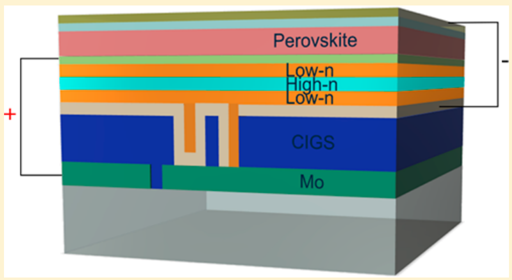

KEYWORDS: *perovskite solar cells, CIGS solar cells, inverse integration, tandem, serial-parallel configuration*

Perovskites (PVKs) recently emerged as a solution-processed PV technology that in a short period of time reached power conversion efficiencies (PCEs) comparable to the ones from the well-established lower band gap crystalline Si technology.[1,2] One of the remarkable features of PVK cells is their high open-circuit voltage (V_{oc}), which may reach values as high as 1.24 V (at a band gap of 1.63 eV).[3] Such high voltages, a tunable band gap,[4] and a high charge mobility make them an optimal technology to form a pair with CIGS or crystalline Si-based solar cells and lead to a low-cost multijunction technology suitable for terrestrial sun energy harvesting.[5−10] In the most standard tandem configuration the two cells are in a serial connection that requires current matching between both cells.[11−14] This constitutes a constraint in the optical design of the optimal tandem architecture that eventually limits the PCE of the final device. To partially circumvent such problems, 3-terminal[15] or 4-terminal[6,13,16,17] configurations have been proposed. The former one is applicable when the two absorber materials are the same, while in the latter one, there are no material constraints. Mechanically stacked 4-terminal devices have shown efficiencies that overcome that of the corresponding single subcells,[6,8] but the monolithic character, which may be relevant to achieve a low-cost solar module installation, would be lost to a large extent. A higher cost associated with the connectivity complexity is expected in the installation of such 4-terminal modules. On a theoretical basis it was proposed to connect an indefinite number of cells in each one of the branches of a parallel configuration in series until the voltages of the two branches are matched.[18] However, no practical implementation of the device configuration was considered. An alternative option proposed piling up three cells, two of them in a series connection and then these two connected in parallel with the remaining one.[19] The latter combination is an interesting proposal to match the voltage, but the problem of current matching remains.

In this work we propose a new configuration, denoted as S-P (serial-parallel), different from the standard or any other tandem scheme considered until now. We describe a monolithic tandem architecture where current matching

Received: November 21, 2016

DOI: 10.1021/acsphotonics.6b00929
ACS Photonics XXXX, XXX, XXX−XXX

between the PVK and CIGS cells is not required. Performing an optical optimization of the structure, we predict an efficiency of 28% using a 1.56 eV band gap PVK and PV parameters that have already been reached for the constituent CIGS or PVK subcells. Furthermore, we discuss the experimental viability of the proposed architecture.

■ RESULTS AND DISCUSSION

As shown in Figure 1a, the configuration is formed with a semitransparent PVK solar cell deposited on top of two CIGS

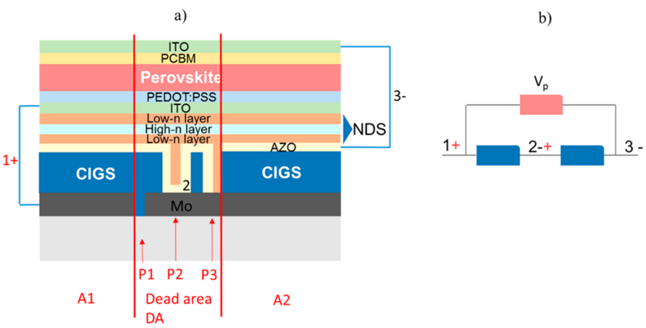

Figure 1. (a) Schematic drawing of the monolithic multijunction device composed of a two-series connected CIGS cell connected in parallel with a PVK cell. (b) Schematic drawing of the connections of the S-P configuration.

solar cells laterally connected in series. A schematic drawing of the architecture with connection nodes numbered from 1 to 3 is shown in Figure 1b. Voltage matching at nodes 1 and 3 from both branches of the circuit may, in principle, be achieved provided the maximum power point voltage (V_{mpp}) of the light-filtered CIGS cells is close to half that from the PVK cell. The serial connection among the two CIGS cells can be implemented by means of laser scribing, a standard technique for the up-scaling of CIGS cells to modules. As seen in Figure 1a, a dielectric multilayer referred as a 1-D photonic nonperiodic dielectric structure (NDS) is inserted on top of the first CIGS solar cell serving the double purpose of avoiding short-circuiting of nodes 1 and 2 and maximizing light absorption for the first and second cell. On the other hand, the necessary current matching between the two serial-connected CIGS devices can be easily obtained by defining an equal area for both.

In the implementation of the optical optimization described in the Methods we consider a configuration where the CIGS solar cell architecture is the standard one and some changes are introduced to the PVK device, for instance, the use of top and bottom transparent conductive electrodes (TEs). Specifically, the S-P architecture consists of the semitransparent PVK cell on top of a CIGS cell separated by the NDS as follows: glass/Mo/MoSe/CIGS/CdS/i-ZnO/AZO/low-*n* film/high-*n* film/low-*n* film/TE/PEDOT:PSS/PVK/PCBM/TE/MgF_2. As TEs for the semitransparent PVK we considered 90 nm ITO films. The ITO is chosen instead of the common FTO due to its better processing compatibility with the underlying materials and its improved near-infrared transmission. Similar thicknesses of ITO films, prepared at room temperature, have been employed to form a recombination layer and top contact in a monolithic tandem architecture with PVK and silicon, exhibiting high fill factors.[10]

In the S-P configuration considered here, the optical optimization is performed for a device that includes the NDS between the inner TE/AZO interface as seen in Figure 1a. Such NDS is formed by a combination of three layers of intercalated low and high refractive index materials and has a 2-fold functionality. First, it electrically separates the TE anode of the PVK and the AZO cathode from the CIGS, and second, it confines the incident sunlight above the PVK band gap in the PVK absorber layer, while increasing the transparency for sunlight below the PVK band gap for an efficient coupling into the CIGS bottom cell. To prevent tunnelling from electrical charges between the PVK and CIGS cells, one may use MgF_2 as a low-*n* material, which is a highly insulating transparent material exhibiting a refractive index close to 1.38. For the high-*n* film, a highly transparent dielectric material with a refractive index of 2.2 would be the optimal. Possible materials for the high-index layer may be TiO_2 or Si_3N_4. Considering the three films, the total thickness of the NDS would be above 500 nm, sufficient, in principle, to prevent electrical charge tunnelling. When the inverse integration optical optimization detailed in the Methods section is applied, the EQEs obtained for the NDS-separated PVK and CIGS cells are shown in Figure 2a. Under the assumption of a negligible extinction coefficient for any of the layers within the NDS, we observe an enhancement in the maximum short-circuit current of the PVK and CIGS subcells, especially in the wavelength range between 700 and 900 nm. The NDS fine-tuning required to reach maximum

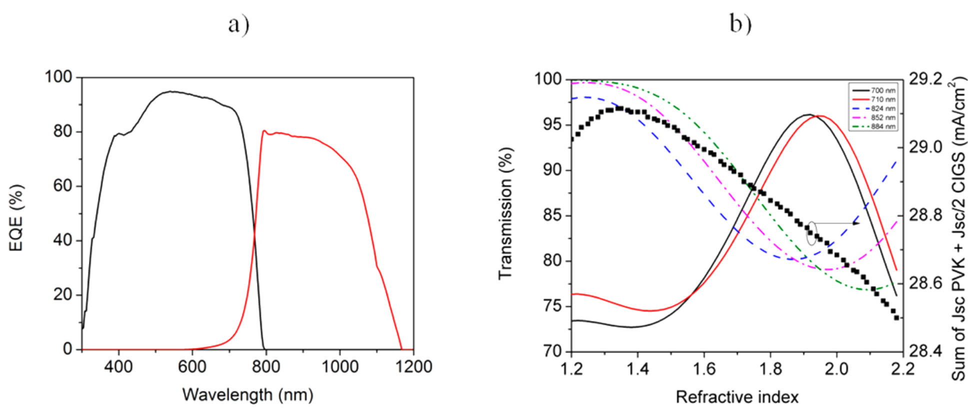

Figure 2. (a) Calculated EQE for the perovskite (black) and the CIGS (red) subcells for the optimal configuration. (b) Sum of PVK and CIGS photocurrent densities (black squares) and transmission of the NDS at 700 nm (black line), 710 nm (red), 824 nm (blue dash), 852 nm (magenta dash dot), and 884 nm (green dash dot dot) as a function of the refractive index of the low-*n* NDS layer.

DOI: 10.1021/acsphotonics.6b00929
ACS Photonics XXXX, XXX, XXX−XXX

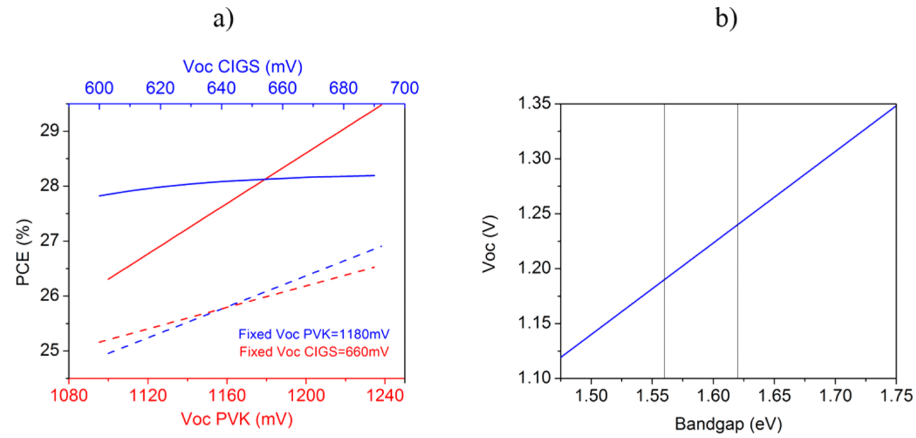

Figure 3. (a) PCEs for the tandem (dashed lines) and S-P (continuous lines) configurations. The red lines correspond to a fixed V_{oc} for the CIGS solar cells at 660 mV, while the V_{oc} of the PVK is allowed to change from 1080 to 1240 mV. The blue lines correspond to a fixed V_{oc} condition of the PVK at 1180 mV, while the V_{oc} of the CIGS is allowed to change from 600 to 690 mV. (b) Estimate of PVK V_{oc} as a function of the PVK band gap. The two reference values are marked as vertical lines.

PCE may be extracted from Figure 2b, where the transmission at five different wavelengths just above and below the PVK band gap is shown as a function of the NDS low refractive index material. In this figure one observes that for the cell architecture with the highest short-circuit current sum, when the NDS low-index material is close to 1.38, the inverse integration leads to an NDS transmission that is larger at longer wavelengths to favor absorption at the CIGS and smaller at shorter wavelengths to favor absorption in the PVK. Note that the unbalanced current density in both subcells explains why the PCE of the S-P configuration is considerably larger than the PCE for the current matched tandem, as seen in Figure 3a. The optimal thicknesses for the critical layers inside the S-P structure depend on the selected TE. When using a 90 nm indium tin oxide (ITO) film, the optimal architecture is glass/Mo/MoSe/CIGS (2.5 μm)/CdS (40 nm)/i-ZnO(50 nm)/AZO(100 nm)/low-*n* film (70 nm)/high-*n* film (220 nm)/low-*n* film (250 nm)/ITO (90 nm)/PEDOT:PSS (20 nm)/PVK (700 nm)/PCBM (20 nm)/ITO (90 nm)/MgF_2 (98 nm), delivering a J_{sc} of 22.06 mA/cm^2 for the PVK and 14.1 mA/cm^2 for the CIGS.

To confirm that such an increase in photocurrent in the S-P configuration corresponds to an equivalent increase in PCE, we determined the rest of the electrical parameters that characterize the overall *IV* curves employing the single-diode electrical equivalent circuit model. The single-diode circuit model was applied to each branch of the circuit, and then the currents were added point by point to obtain the resulting *IV* curve. To reach optimal PCEs, we set the fill factor (FF) between 80% and 81% for all the single-junction cells used in the S-P configuration. A similar procedure was used to determine the optimal configuration for a standard current-matched tandem, which is used as a reference for comparison. Although small variations resulting from the *IV* curve fitting may be found, the FF of the S-P structure closely approached that of the subcell, with the highest FF for most of the cases considered. On the other hand, the V_{oc} of the S-P is roughly limited by the voltage of the branch that has the lowest voltage, as can be seen in Figure S1 of the SI. We studied two cases, one where the V_{oc} of the PVK was fixed to 1180 mV while the V_{oc} of the CIGS was varied in the 600−700 mV range, and a second case where the V_{oc} of the CIGS was fixed to 660 mV and that of the PVK was allowed to change in the 1080−1240 mV range. The ideality factor, series resistance, shunt resistance, and saturation current were determined to match experimental curves when available (Figure S2 of the SI) or from the computer-generated single-junction *IV* curves exhibiting the targeted J_{sc}, FF, and V_{oc} parameters. Note that the changes in V_{oc} considered here are not associated with band gap modifications, which will be considered below. Indeed the V_{oc} ranges encompass a wide variety of voltages that are often found in experimental CIGS or PVK single-junction devices.

As seen in Figure 3a, when a PVK cell with a V_{oc} of 1180 mV is combined with a CIGS cell in the S-P configuration, the efficiency remains more or less around 28% as the V_{oc} of the CIGS changes. This PCE is clearly larger than the PCE from any of the possible tandem configurations also shown in Figure 3a. In the event that the V_{oc} of the PVK is further increased, PCEs above 29% would be reachable, while for the standard tandem PCEs larger than 27% are, in principle, not possible. This confirms that the S-P configuration clearly outperforms the standard tandem by more than two percentage points in almost all cases. Note that, when optimal single-junction cells are considered, both configurations, tandem and S−P, will clearly outperform record PCEs for CIGS[20] and PVK[21] single-junction cells.

Provided that in the S-P configuration no current matching is required between the PVK and the CIGS cells, a further increase in the PCE may be achieved by tuning the band gap of either the PVK or CIGS cells. For PVK cells several authors have considered tuning the band gap by changing the relative halide composition and observed an increase in the V_{oc}. Although in most cases studied no clear relationship was established between the V_{oc} and the band gap, from the wide band gap tuning study reported by Noh et al.[4] one may extract a close to linear correspondence between these two parameters when the band gap is changed from 1.57 to 2.29 eV. The V_{oc} values therein reported are, however, low in comparison to recent reports. For instance, PVK cells with a measured band gap of 1.56 eV have reached a V_{oc} as high as 1.19 V.[22] Similarly, for a higher band gap PVK of 1.62 eV, a V_{oc} of 1.24 eV[3] was recently achieved, which corresponds to a loss in potential (difference band gap and V_{oc}) of 0.39 eV, which is close to the thermodynamic limit. Thus, an increase in V_{oc} may be achievable for the other band gaps as well once the charge extraction contacts and the perovskite composition have been

DOI: 10.1021/acsphotonics.6b00929
ACS Photonics XXXX, XXX, XXX−XXX

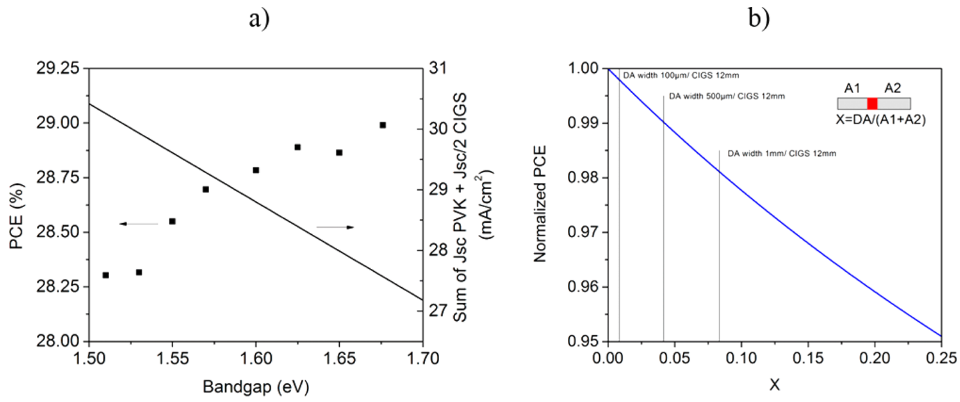

Figure 4. (a) PCE of the CIGS/PVK S-P cells as a function of the PVK band gap (squares) and sum of PVK and CIGS halved short-circuit current densities for the S-P configuration as a function of the PVK band gap (line). (b) PCE as a function of DA width of the serial-connected cells assuming devices with an area of 12 × 12 mm^2.

optimized to overcome limiting effects such as the one described in ref 23. For this work, the above two values are taken as references and used to establish a linear relation between the V_{oc} and the band gap in the range of 1.51 to 1.71 eV, shown in Figure 3b. At present, there are material compositions for PVK cells yielding band gaps below 1.56 eV.[13,24,25] However, such compositions have led to suboptimal devices, which were not taken as references for this analysis. A monotonic decrease of the total calculated short-circuit current density as the band gap increases is observed in Figure 4a. Note that we have plotted the sum of the short-circuit current density of the PVK with half of the CIGS to account for the differences in area inherent to the S-P structure. When estimating the PCE using the same single-diode model described above, one observes, as can be seen in Figure 4a, an increase in PCE as the band gap of the PVK increases. Although this may seem counterintuitive provided the band gap of PVK is well above the optimal single-junction solar cell band gap, the explanation is that the band gap increase implies a better voltage matching with the CIGS branch of the circuit.

■ METHODS

Intercalated Nonperiodic Photonic Structure for Optimal Light Harvesting. To design the specific architecture for the S-P cell, we set the sum of the photocurrents as the target optimization parameter within our numerical calculations.

From Figure 1b, it can be seen that the maximum electrical power P derived from the device is given by

$$P = (I_{CIGS} + I_{PVK})V_p \times FF \quad (1)$$

,where I_{CIGS} is the short-circuit current generated by the CIGS solar cell and I_{PVK} is the short-circuit current generated by the PVK. V_p and FF are the corresponding voltage and fill factor from the parallel connection.

$$I_{PVK} = J_{PVK}(A_T) \quad (2)$$

with J_{PVK} being the short-circuit current density from the PVK and A_T the total illumination area of the device. Neglecting the dead area, A_T corresponds to

$$A_T = A_1 + A_2 \quad (3)$$

where A_1 and A_2 are the areas for the CIGS subcells (for practical considerations refer to the next subsection). The current flowing through the CIGS cells must fulfill

$$I_{CIGS} = A_1 J_{CIGS1} = A_2 J_{CIGS2} \quad (4)$$

By simple algebra one may write the PCE as

$$PCE = \frac{[(A_1 J_{CIGS1}) + (A_T J_{PVK})]V_p \times FF}{P_{AM1.5} A_T} \quad (5)$$

We determine the optimal cell architecture by implementing an inverse integration approach where the photocurrent from each one of a large set of possible configuration solutions is numerically computed using a transfer matrix formalism. Configurations are defined by a large set of different input parameters, including thicknesses and/or optical constants for some or all the device layers, which are allowed to vary within a specified range. The target solution is selected from that set of all possible solutions.

When implementing the transfer matrix model, it is assumed that all layers are considered homogeneous and isotropic, such that their optical characteristics can be represented by scalar complex indexes of refraction; interfaces between adjacent layers are parallel and optically flat; incident light is perpendicular to the stack and can be described by plane waves; and the efficiencies in exciton diffusion, charge separation, and carrier transport and collection are wavelength independent. To perform these calculations, one must know the complex index of refraction and thickness for each layer in the architecture. The refractive indexes for each layer were taken from refs 26 and 27 for the CIGS solar cell and from refs 28 and 29 for most of the layers in the PVK solar cell.

Using the calculated electric field intensities for the CIGS and PVK, together with their optical properties, the absorption is computed to finally determine the short-circuit current density (J_{sc}) for each subcell. J_{sc}'s for the PVK and CIGS cells were computed for 10 000 different combinations of layer thicknesses when varying the absorber layers, the entrance transparent electrode, and the intermediate dielectric NDS layers. The thickness ranges were in accordance with the experimental constraints to obtain an optimal FF or V_{oc} for both cells. We assumed an internal quantum efficiency (IQE) of 100% for the PVK cell, as demonstrated in refs 30 and 31 and 92% for the CIGS solar cells.[32] In the PCE estimates, we obtained the equivalent parallel voltage V_p and FF by adding

DOI: 10.1021/acsphotonics.6b00929
ACS Photonics XXXX, XXX, XXX−XXX

the *IV* curves corresponding to each one of the branches of the circuit.

Experimental Implementation of S-P Structure. The CIGS bottom cells in this design can be deposited in the different ways described in the literature, since there are no special limitations on process temperature or conditions present at this point. In order to reach the desired efficiency, a deposition by co-evaporation or precursor selenization seems to be favorable. The substrate can be rigid (soda lime glass) or flexible (polyimides, steel), especially in view of possible roll-to-roll production. The back contact is typically Mo around 500 nm. The absorber will be between 2 and 3 μm thick, followed by a buffer layer (most likely CdS by chemical bath deposition) and a multilayer of intrinsic and doped zinc oxide as TE. The front contact sheet resistance should be below 10 ohm/sq for a monolithic cell interconnection.

Concerning the fabrication of the PVK device on top of the CIGS, a number of constraints are introduced to prevent damage of the bottom CIGS layer. For instance, thermal instability has been observed for the n-type buffer layer in CIGS solar cells, where atoms tend to diffuse from the buffer to the absorber layer, significantly reducing the performance of the device by an augmented recombination. Temperatures above 300 °C trigger this process and have been shown to be detrimental to all PV parameters of CIGS solar cells.[33] Therefore, annealing processes used to manufacture all the layers within the PVK device are temperature-limited, which excludes the use of frequent configurations such as the mesoscopic PVK on 500 °C sintered TiO_2. The PVK layer itself does not require high-temperature annealing and neither does the PCBM. On the other hand, ITO has been shown to provide good-quality transparent electrodes at the bottom or the top of PVK solar cells.[10,34] Connection of PVK cells to modules has been reported in the literature,[35] some with a reduced area loss of 3% of the total 16 cm^2 module area.[36]

Similarly to the case of PVK, for the lateral serial connection of the CIGS solar cells three structured patterns denominated P1, P2, and P3 are required, as seen in Figure 1a. The first pattern, P1, and the third pattern, P3, separate the positive and negative contacts of adjacent cells, respectively. The second pattern, P2, allows the negative contact of one cell to be connected with the positive contact of the following cell. The region in between P1 and P3, including both, is the dead area (DA). Typically, laser scribing is employed to define such patterns. If we assume that the dead area corresponds to a fraction *X* of the total CIGS active cell area, then

$$DA = X(A_1 + A_2) \tag{6}$$

Within the optically optimized S-P structure we consider the effect of the DA in the total PCE by normalizing it without neglecting the DA. As can be seen in Figure 4b, under the assumption of a cell larger than 1 cm, the effective loss in PCE is less than 2% even when the separation between P1 and P3, including the width of such laser cuts, is as large as 500 μm. For separations as small as 100 μm, which have been recently outperformed in the series connection of CIGS cells,[37] the loss in PCE is negligible.

■ CONCLUSIONS

In summary, we proposed and studied a new tandem configuration where the constraint of current density matching is removed. Two CIGS cells laterally connected in series may be connected in parallel with a PVK cell matching the maximum power point voltages. The configuration studied is monolithic, but the currents from the top PVK and the bottom CIGS cells can be extracted separately. We demonstrated that when the two cells are electrically separated by a dielectric nonperiodic photonic multilayer structure, such photonic structure can be designed to effectively confine the incident sun light above the PVK band gap in the PVK absorber layer. The same photonic structure is used to reach an optimal transparency for sunlight below this band gap and efficiently couple it into the CIGS bottom cell. Using realistic current state-of-the-art parameters for all layers in the multijunction architecture we estimated that PCEs above 28% can be achieved. The PCE of the S-P configuration is for most of the cases studied two percentage points higher in efficiency than that estimated for an optimal series-connected standard tandem configuration or 22.6% and 22.1%, which are the maximum efficiencies reported for CIGS and PVK single-junction cells, respectively. Any improvement in the subcells will further increase the potential efficiency of the S-P cell. For a successful experimental implementation of the S-P configuration, the procedures to fabricate high-quality semitransparent electrodes with the limitations imposed by the layers already deposited must be improved. In addition, the optical optimization of the NDS must be made compatible with its role of preventing short-circuiting between the two subcells.

■ ASSOCIATED CONTENT

Supporting Information

The Supporting Information is available free of charge on the ACS Publications website at DOI: 10.1021/acsphotonics.6b00929.

Curve of equivalent V_{oc} for the S-P configuration when varying the V_{oc} of the PVK subcell or V_{oc} of the CIGS subcell; fitting data of *IV* curves; module interconnection schemes for the S-P configuration (PDF)

■ AUTHOR INFORMATION

Corresponding Author

*E-mail: paola.mantilla@icfo.es.

ORCID

Paola Mantilla-Perez: 0000-0003-4801-4949
Juan-Pablo Correa-Baena: 0000-0002-3860-1149
Johann Toudert: 0000-0002-1609-1934

Notes

The authors declare no competing financial interest.

■ ACKNOWLEDGMENTS

P.M.P., Q.L., S.C., J.T., and J.M. acknowledge financial support from the Spanish MINECO (Severo Ochoa program, grant no. SEV-2015-0522), the MINECO, the Fondo Europeo de Desarrollo Regional FEDER (grant no. MAT2014-52985-R), the Fundació Privada Cellex, and the EC FP7 Program (ICT-2011.35) under grant agreement no. NMP3-SL-2013-604506. M.S. acknowledges support from the cofunded Marie Skłodowska Curie fellowship, H2020 grant agreement no. 665667. Financial funding from the Swiss National Science Foundation (SNF)-NanoTera as well as Competence Center for Energy and Mobility (CCEM Connect-PV) is gratefully acknowledged.

■ REFERENCES

(1) Battaglia, C.; Cuevas, A.; De Wolf, S. High-Efficiency Crystalline Silicon Solar Cells: Status and Perspectives. *Energy Environ. Sci.* **2016**, *9*, 1552−1576.

(2) Saliba, M.; Matsui, T.; Seo, J.; Domanski, K.; Correa-Baena, J.; Nazeeruddin, M.; Zakeeruddin, S.; Tress, W.; Abate, A.; Hagfeldt, A.; Grätzel, M. Cesium-Containing Triple Cation Perovskite Solar Cells: Improved Stability, Reproducibility and High Efficiency. *Energy Environ. Sci.* **2016**, *9*, 1989−1997.

(3) Saliba, M.; Matsui, T.; Domanski, K.; Seo, J.; Ummadisingu, A.; Zakeeruddin, S.; Correa-Baena, J.; Tress, W.; Abate, A.; Hagfeldt, A.; Grätzel, M. Incorporation of Rubidium Cations into Perovskite Solar Cells Improves Photovoltaic Performance. *Science* **2016**, *354*, 206−209.

(4) Noh, J.; Im, S.; Heo, J.; Mandal, T.; Seok, S. Chemical Management for Colorful, Efficient, and Stable Inorganic−Organic Hybrid Nanostructured Solar Cells. *Nano Lett.* **2013**, *13*, 1764−1769.

(5) Todorov, T.; Gershon, T.; Gunawan, O.; Lee, Y.; Sturdevant, C.; Chang, L.; Guha, S. Monolithic Perovskite-CIGS Tandem Solar Cells Via In Situ Bandgap Engineering. *Adv. Energy Mater.* **2015**, *5*, 1500799.

(6) Kranz, L.; Abate, A.; Feurer, T.; Fu, F.; Avancini, E.; Löckinger, J.; Reinhard, P.; Zakeeruddin, S.; Grätzel, M.; Buecheler, S.; Tiwari, A. High-Efficiency Polycrystalline Thin Film Tandem Solar Cells. *J. Phys. Chem. Lett.* **2015**, *6*, 2676−2681.

(7) McMeekin, D.; Sadoughi, G.; Rehman, W.; Eperon, G.; Saliba, M.; Horantner, M.; Haghighirad, A.; Sakai, N.; Korte, L.; Rech, B.; Johnston, M. B.; Herz, L. M.; Snaith, H. J. A Mixed-Cation Lead Mixed-Halide Perovskite Absorber for Tandem Solar Cells. *Science* **2016**, *351*, 151−155.

(8) Bailie, C.; Christoforo, M.; Mailoa, J.; Bowring, A.; Unger, E.; Nguyen, W.; Burschka, J.; Pellet, N.; Lee, J.; Grätzel, M.; Noufi, R.; Buonassisi, T.; Salleo, A.; McGehee, M. D. Semi-Transparent Perovskite Solar Cells for Tandems with Silicon and CIGS. *Energy Environ. Sci.* **2015**, *8*, 956−963.

(9) Mailoa, J.; Bailie, C.; Johlin, E.; Hoke, E.; Akey, A.; Nguyen, W.; McGehee, M.; Buonassisi, T. A. 2-Terminal Perovskite/Silicon Multijunction Solar Cell Enabled by a Silicon Tunnel Junction. *Appl. Phys. Lett.* **2015**, *106*, 121105.

(10) Albrecht, S.; Saliba, M.; Correa Baena, J.; Lang, F.; Kegelmann, L.; Mews, M.; Steier, L.; Abate, A.; Rappich, J.; Korte, L.; Schlatmann, R.; Nazeeruddin, M. K.; Hagfeldt, A.; Grätzel, M.; Rech, B. Monolithic Perovskite/Silicon-Heterojunction Tandem Solar Cells Processed at Low Temperature. *Energy Environ. Sci.* **2016**, *9*, 81−88.

(11) Todorov, T.; Gershon, T.; Gunawan, O.; Sturdevant, C.; Guha, S. Perovskite-Kesterite Monolithic Tandem Solar Cells with High Open-Circuit Voltage. *Appl. Phys. Lett.* **2014**, *105*, 173902.

(12) Reinhard, M.; Sonntag, P.; Eckstein, R.; Bürkert, L.; Bauer, A.; Dimmler, B.; Lemmer, U.; Colsmann, A. Monolithic Hybrid Tandem Solar Cells Comprising Copper Indium Gallium Diselenide and Organic Sub-cells. *Appl. Phys. Lett.* **2013**, *103*, 143904.

(13) Eperon, G.; Leijtens, T.; Bush, K.; Prasanna, R.; Green, T.; Wang, J.; McMeekin, D.; Volonakis, G.; Milot, R.; May, R.; Palmstrom, A.; Slotcavage, D. J.; Belisle, R. A.; Patel, J. B.; Parrott, E. S.; Sutton, R. J.; Ma, W.; Moghadam, F.; Conings, B.; Babayigit, A.; Boyen, H.-G.; Bent, Stacey; Giustino, F.; Herz, L. M.; Johnston, M. B.; McGehee, M. D.; Snaith, H. J. Perovskite-Perovskite Tandem Photovoltaics with Optimized Bandgaps. *Science* **2016**, *354*, 861.

(14) Chae, S.; Park, S.; Joo, O.; Jun, Y.; Min, B.; Hwang, Y. Highly Stable Tandem Solar Cell Monolithically Integrating Dye-Sensitized and CIGS Solar Cells. *Sci. Rep.* **2016**, *6*, 30868.

(15) Sista, S.; Hong, Z.; Park, M.; Xu, Z.; Yang, Y. High-Efficiency Polymer Tandem Solar Cells With Three-Terminal Structure. *Adv. Mater.* **2010**, *22*, E77−E80.

(16) Löper, P.; Moon, S.; Martín de Nicolas, S.; Niesen, B.; Ledinsky, M.; Nicolay, S.; Bailat, J.; Yum, J.; De Wolf, S.; Ballif, C. Organic−Inorganic Halide Perovskite/Crystalline Silicon Four-Terminal Tandem Solar Cells. *Phys. Chem. Chem. Phys.* **2015**, *17*, 1619−1629.

(17) Fu, F.; Feurer, T.; Jäger, T.; Avancini, E.; Bissig, B.; Yoon, S.; Buecheler, S.; Tiwari, A. Low-Temperature-Processed Efficient Semi-Transparent Planar Perovskite Solar Cells For Bifacial and Tandem Applications. *Nat. Commun.* **2015**, *6*, 8932.

(18) Strandberg, R. Detailed Balance Analysis of Area De-Coupled Double Tandem Photovoltaic Modules. *Appl. Phys. Lett.* **2015**, *106*, 033902.

(19) Guo, F.; Li, N.; Fecher, F.; Gasparini, N.; Quiroz, C.; Bronnbauer, C.; Hou, Y.; Radmilović, V.; Radmilović, V.; Spiecker, E.; Forberich, K.; Brabec, C. J. A Generic Concept to Overcome Bandgap Limitations for Designing Highly Efficient Multi-Junction Photovoltaic Cells. *Nat. Commun.* **2015**, *6*, 7730.

(20) Jackson, P.; Wuerz, R.; Hariskos, D.; Lotter, E.; Witte, W.; Powalla, M. Effects of Heavy Alkali Elements in Cu(In,Ga)Se2 Solar Cells with Efficiencies up to 22.6%. *Phys. Status Solidi RRL* **2016**, *10*, 583−586.

(21) National Renewable Energy Laboratory, Best Research-Cell Efficiencies chart; www.nrel.gov/ncpv/images/efficiency_chart.jpg.

(22) Correa Baena, J.; Steier, L.; Tress, W.; Saliba, M.; Neutzner, S.; Matsui, T.; Giordano, F.; Jacobsson, T.; Srimath Kandada, A.; Zakeeruddin, S.; Petrozza, A.; Abate, A.; Nazeeruddin, M. K.; Grätzel, M.; Hagfeldt, A. Highly Efficient Planar Perovskite Solar Cells Through Band Alignment Engineering. *Energy Environ. Sci.* **2015**, *8*, 2928−2934.

(23) Slotcavage, D.; Karunadasa, H.; McGehee, M. Light-Induced Phase Segregation in Halide-Perovskite Absorbers. *ACS Energy Lett.* **2016**, *1*, 1199−1205.

(24) Filip, M.; Eperon, G.; Snaith, H.; Giustino, F. Steric Engineering of Metal-Halide Perovskites with Tunable Optical Bandgaps. *Nat. Commun.* **2014**, *5*, 5757.

(25) Yang, Z.; Rajagopal, A.; Chueh, C.; Jo, S.; Liu, B.; Zhao, T.; Jen, A. Stable Low-Bandgap Pb-Sn Binary Perovskites for Tandem Solar Cells. *Adv. Mater.* **2016**, *28*, 8990−8997.

(26) Hara, T.; Maekawa, T.; Minoura, S.; Sago, Y.; Niki, S.; Fujiwara, H. Quantitative Assessment of Optical Gain and Loss in Submicron-Textured $CuIn_{(1-x)}Ga_xSe_2$ Solar Cells Fabricated by Three-Stage Coevaporation. *Phys. Rev. Appl.* **2014**, *2*.10.1103/PhysRevApplied.2.034012

(27) Macco, B.; Wu, Y.; Vanhemel, D.; Kessels, W. High Mobility In2O3:H Transparent Conductive Oxides Prepared by Atomic Layer Deposition and Solid Phase Crystallization. *Phys. Status Solidi RRL* **2014**, *8*, 987−990.

(28) Correa-Baena, J.; Anaya, M.; Lozano, G.; Tress, W.; Domanski, K.; Saliba, M.; Matsui, T.; Jacobsson, T. J.; Calvo, M. E.; Abate, A.; Grätzel, M.; Míguez, H.; Hagfeldt, A. Unbroken Perovskite: Interplay of Morphology, Electrooptical Properties, and Ionic Movement. *Adv. Mater.* **2016**, *28*, 5031−5037.

(29) Chen, C.; Hsiao, S.; Chen, C.; Kang, H.; Huang, Z.; Lin, H. Optical Properties of Organometal Halide Perovskite Thin Films and General Device Structure Design Rules for Perovskite Single and Tandem Solar Cells. *J. Mater. Chem. A* **2015**, *3*, 9152−9159.

(30) Yang, B.; Dyck, O.; Poplawsky, J.; Keum, J.; Puretzky, A.; Das, S.; Ivanov, I.; Rouleau, C.; Duscher, G.; Geohegan, D.; Xiao, K. Perovskite Solar Cells with Near 100% Internal Quantum Efficiency Based on Large Single Crystalline Grains and Vertical Bulk Heterojunctions. *J. Am. Chem. Soc.* **2015**, *137*, 9210−9213.

(31) Lin, Q.; Armin, A.; Nagiri, R.; Burn, P.; Meredith, P. Electro-Optics of Perovskite Solar Cells. *Nat. Photonics* **2014**, *9*, 106−112.

(32) Pettersson, J.; Torndahl, T.; Platzer-Björkman, C.; Hulqvist, A.; Edoff, M. The Influence of Absorber Thickness on Cu(In, Ga)Se2 Solar Cells with Different Buffer Layers. *IEEE J. Photovolt.* **2013**, *3*, 3.

(33) Wi, J.; Kim, T.; Kim, J.; Lee, W.; Cho, D.; Han, W.; Chung, Y. Photovoltaic Performance and Interface Behaviors of Cu(In,Ga)Se 2 Solar Cells With a Sputtered-Zn(O,S) Buffer Layer by High-Temperature Annealing. *ACS Appl. Mater. Interfaces* **2015**, *7*, 17425−17432.

(34) Duong, T.; Lal, N.; Grant, D.; Jacobs, D.; Zheng, P.; Rahman, S.; Shen, H.; Stocks, M.; Blakers, A.; Weber, K.; White, T. P.; Catchpole, K. R. Semitransparent Perovskite Solar Cell with Sputtered Front and Rear Electrodes for a Four-Terminal Tandem. *IEEE J. Photovolt.* **2016**, *6*, 679−687.

DOI: 10.1021/acsphotonics.6b00929
ACS Photonics XXXX, XXX, XXX−XXX

(35) Fakharuddin, A.; Di Giacomo, F.; Palma, A.; Matteocci, F.; Ahmed, I.; Razza, S.; D'Epifanio, A.; Licoccia, S.; Ismail, J.; Di Carlo, A.; Brown, T. M.; Jose, R. Vertical TiO2 Nanorods as a Medium for Stable and High-Efficiency Perovskite Solar Modules. *ACS Nano* **2015**, *9*, 8420−8429.

(36) Gehlhaar, R.; Merckx, T.; Masse de la Huerta, C.; Qiu, W.; Cheyns, D.; Aernouts, T. Perovskite Solar Modules with Minimal Area Loss Interconnections. *SPIE* Newsroom **2015**, 2/310.1117/2.1201509.006116.

(37) Nishiwaki, S.; Burn, A.; Buecheler, S.; Muralt, M.; Pilz, S.; Romano, V.; Witte, R.; Krainer, L.; Spühler, G.; Tiwari, A. A Monolithically Integrated High-Efficiency Cu(In,Ga)Se_2 Mini-Module Structured Solely by Laser. *Prog. Photovoltaics* **2015**, *23*, 1908−1915.

DOI: 10.1021/acsphotonics.6b00929
ACS Photonics XXXX, XXX, XXX−XXX